ACS APPLIED MATERIALS & INTERFACES

Research Article

www.acsami.org

# Alloyed Crystalline Au–Ag Hollow Nanostructures with High Chemical Stability and Catalytic Performance

Renxiao Liu,[*,†,§] Jianhua Guo,[‡,§] Gang Ma,[‡] Peng Jiang,[*,†] Donghui Zhang,[†] Dexing Li,[†] Lan Chen,[†] Yuting Guo,[†] and Guanglu Ge[*,†]

[†]CAS Key Laboratory of Standardization and Measurement for Nanotechnology, CAS Center for Excellence in Nanoscience, National Center for Nanoscience and Technology, Beijing 100190, P. R. China

[‡]Key Laboratory of Medicinal Chemistry and Molecular Diagnosis of Ministry of Education, College of Chemistry and Environmental Science, Hebei University, Baoding 071002, China

Supporting Information

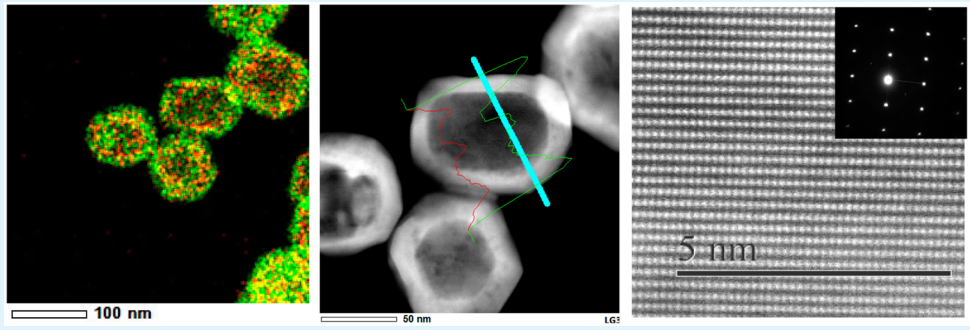


**ABSTRACT:** For bimetallic nanoparticles (NPs), the degree of alloying is beginning to be recognized as a significant factor affecting the NP properties. Here, we report an alloyed crystalline Au–Ag hollow nanostructure that exhibits a high catalytic performance, as well as structural and chemical stability. The Au–Ag alloyed hollow and porous nanoshell structures (HPNSs) with different morphologies and subnanoscale crystalline structures were synthesized by adjusting the size of the sacrificial Ag NPs via a galvanic replacement reaction. The catalytic activities of the nanomaterials were evaluated by the model reaction of the catalytic reduction of *p*-nitrophenol by $NaBH_4$ to *p*-aminophenol. The experimental results show that the subnanoscale crystalline structure of the Au–Ag bimetallic HPNSs has much greater significance than the apparent morphology does in determining the catalytic ability of the nanostructures. The Au–Ag alloyed HPNSs with better surface crystalline alloying microstructures and open morphologies were found to exhibit much higher catalytic reaction rates and better cyclic usage efficiencies, probably because of the better dispersion of active Au atoms within these materials. These galvanic replacement-synthesized alloyed Au–Ag HPNSs, fabricated by a facile method that avoids Ag degradation, have potential applications in catalysis, nanomedicine (especially in drug/gene delivery and cancer theranostics), and biosensing.

**KEYWORDS:** *alloyed crystalline, hollow nanostructures, catalysis, gold, silver*

## INTRODUCTION

Bimetallic nanomaterials (NMs) have attracted increasing attention recently for the novel physical and chemical properties they offer, derived from the synergistic effects of combining different metallic elements.[1−7] Among various bimetallic NMs, Au–Ag alloyed bimetallic nanoparticles (NPs) have been extensively researched because they exhibit unique composition-tunable plasmonics properties applicable to catalysis and sensor systems.[8−11] The most commonly reported structures of bimetallic alloyed NPs have been solid NPs and hollow and porous nanoshell structures (HPNSs).[12−18] For Au–Ag alloyed solid NPs, typical synthesis methods involve the coreduction of $HAuCl_4$ and $AgNO_3$ precursors through the wet-chemical method. However, this method has two critical problems of the coprecipitation of AgCl in water[10,15,19,20] and phase-segregation. Phase segregation causes the enrichment of Ag on the most surface of Au–Ag alloyed NPs because of the different surface energy values of Au (97 meV/Å$^2$) and Ag (78 meV/Å$^2$). Heterogeneity of the NP surface significantly affects the surface-sensitive measurements necessary for diagnostics, catalytic activity, and biocompatibility.[21−24] Rajendra et al.[25] used $NH_4OH$ as an additive to overcome AgCl precipitation to obtain citrate-stabilized homogeneously alloyed Au–Ag NPs. This innovative preparation illuminated the effects of alloying on the surface plasmon resonance (SPR), catalytic ability, and stability. Compared to solid NPs, HPNSs have shown advantages in catalysis and nanomedicine applications because they have increased surface

Received: March 28, 2016
Accepted: June 7, 2016
Published: June 7, 2016





DOI: 10.1021/acsami.6b03728
ACS Appl. Mater. Interfaces 2016, 8, 16833−16844

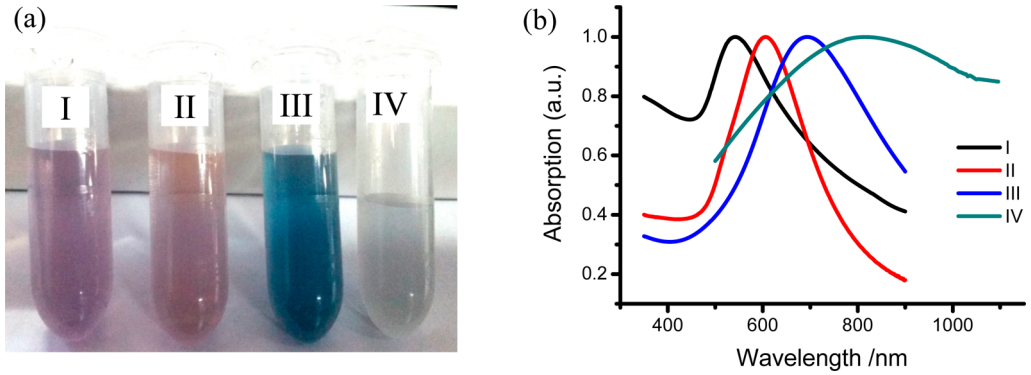


**Figure 1.** (a) Digital photos and (b) UV−vis absorption spectra of (I) AuAg540, (II) AuAg600, (III) AuAg696, and (IV) AuAg813. The size of sacrificial Ag NPs is ∼60−70 (for II), ∼70−80 (for I and III), and ∼80−90 nm (for IV). The concentration of Au is equal to 0.1 mM for each sample.

area, lower masses, and broadly tunable plasmonics wavelengths. Previous studies proved that the metallic HPNSs exhibited catalytic activity superior to that of solid NPs because of the more open morphologies.[26,27] Xia et al.[28] demonstrated that both the porosity and wall thickness of Au-based nanocages and nanoboxes were important in enhancing the catalytic activity of the structures. Wu et al.[29] investigated the catalytic activity of similarly sized HPNSs with differing degrees of structural openness, finding that the morphology, or porosity, of the HPNSs was the most important factor in the catalytic abilities of Au−Ag alloyed HPNSs. The HPNSs in these studies were mostly synthesized through galvanic replacement reactions. However, it is widely recognized that galvanic replacement leads inevitably to dealloying with the continuous addition of $HAuCl_4$, meaning that the Ag within the alloyed HPNSs was unstable and easily degraded.[16]

The distributions of Au and Ag atoms within the alloyed HPNSs were regarded as uncontrollable within randomly alloyed structures.[30] With this perspective, the degradation of Ag seemed inevitable, and reported works on Au−Ag alloyed HPNSs did not focus on the atomic-scale coexistence of Au and Ag. The effects of Ag degradation and lattice structure instability on the physicochemical and catalytic properties of HPNSs have not yet been investigated. In fact, the problem of Ag degradation[31] may have serious impacts. One severe challenge of implementing Ag-containing NPs practically was overcoming biological toxicity. Two methods were attempted to solve this problem: total removal of Ag by etching with excess $H_2O_2$[32] or inhibition of Ag degradation by surface modification with large polymer molecules.[33]

Here, we found that the coexistence of Au and Ag in the NPs significantly affected the structural and chemical stability, which are very important in determining the catalytic properties of Au−Ag alloyed HPNSs.[16,29] A significant improvement in the structural and chemical stability could be achieved by adjusting the size of the sacrificial Ag NPs. The alloying in this exploration deepens our understanding of the replacement reaction and may provide new candidates for alloying-tuned bimetallic nanostructures with improved functions.

## RESULTS AND DISCUSSION

**HPNSs.** In a typical galvanic replacement reaction between Ag nanostructures and $HAuCl_4$ in an aqueous medium,[16] the nanostructure, involving hollow interiors, smooth surfaces, and homogeneous walls consisting of the Au−Ag alloys would be formed in the first step. This structure would be dealloyed as the replacement reaction proceeded with the continuous addition of $HAuCl_4$, finally yielding porous nanostructures. The occurrence of dealloying indicated the instability of Ag within the homogeneous alloyed Au/Ag walls.

By variation of the average size of the sacrificial Ag NPs, four kinds of Au−Ag alloyed NPs with different morphologies and crystalline structures were synthesized. The four samples exhibited different colors of scattering light and different SPR peak wavelengths (Figure 1), demonstrating the distinct differences in size and morphology among the samples. From both TEM and SEM images (Figure 2) and ICP-MS analysis (Table 1), the morphologies and elemental contents of the samples were recognized and quantified.

**AuAg540 NPs.** The morphology of AuAg540 is shown as solid Au−Ag alloyed NPs with irregular shapes. The Au/Ag atomic ratio is ∼5:1 according to ICP-MS (Table 1). From the HRTEM images, a crystal lattice structure with a high degree of crystallization is observed, with a lattice spacing of 2.383 Å (distance between (111) planes). The crystal lattice structure corresponding to the (111) facet is confirmed by the SAED pattern in Figure 2.

**AuAg600 NPs.** AuAg600 is composed of hollow crystalline Au−Ag alloyed HPNSs with smooth surfaces and thick compact walls with no obvious pinholes in the outer surfaces, as shown in Figure 2. The Au/Ag atomic ratio is ∼3:2 according to the ICP-MS results (Table 1). The SAED pattern exhibits a crystalline microstructure. From the experimental phenomena and characterization results, AuAg600 is a stable and homogeneous solid-solution alloy. As shown in Figure 3b, the material is structurally and chemically stable from experimental phenomena based on the SPR peak reaching a maximum red-shifted wavelength of 600 nm, despite the addition of excess $HAuCl_4$. This indicates that the remaining Ag atoms were no longer replaced with Au. In addition, the SPR peak wavelength of 600 nm remains constant with etching by $H_2O_2$ + $NH_4OH$, with the exception of a slight decrease in absorption intensity after 18h etching treatment. Even with etching using 25 mM $H_2O_2$, the morphologies of the Au−Ag alloyed NPs remain unchanged except the disappearance of small Ag-containing NPs, as shown in the STEM images in Figure 4a and 4d. The Au and Ag atoms maintain coexistence in the compact walls, and the atomic distribution of both elements is homogeneous as demonstrated by both HADDF elemental mapping and cross-sectional compositional line-scan EDS spectra for arbitrary HPNSs, as shown in Figure 4b, 4c, 4e, and 4f. From the HADDF mapping images, it is obvious that


DOI: 10.1021/acsami.6b03728
ACS Appl. Mater. Interfaces 2016, 8, 16833−16844

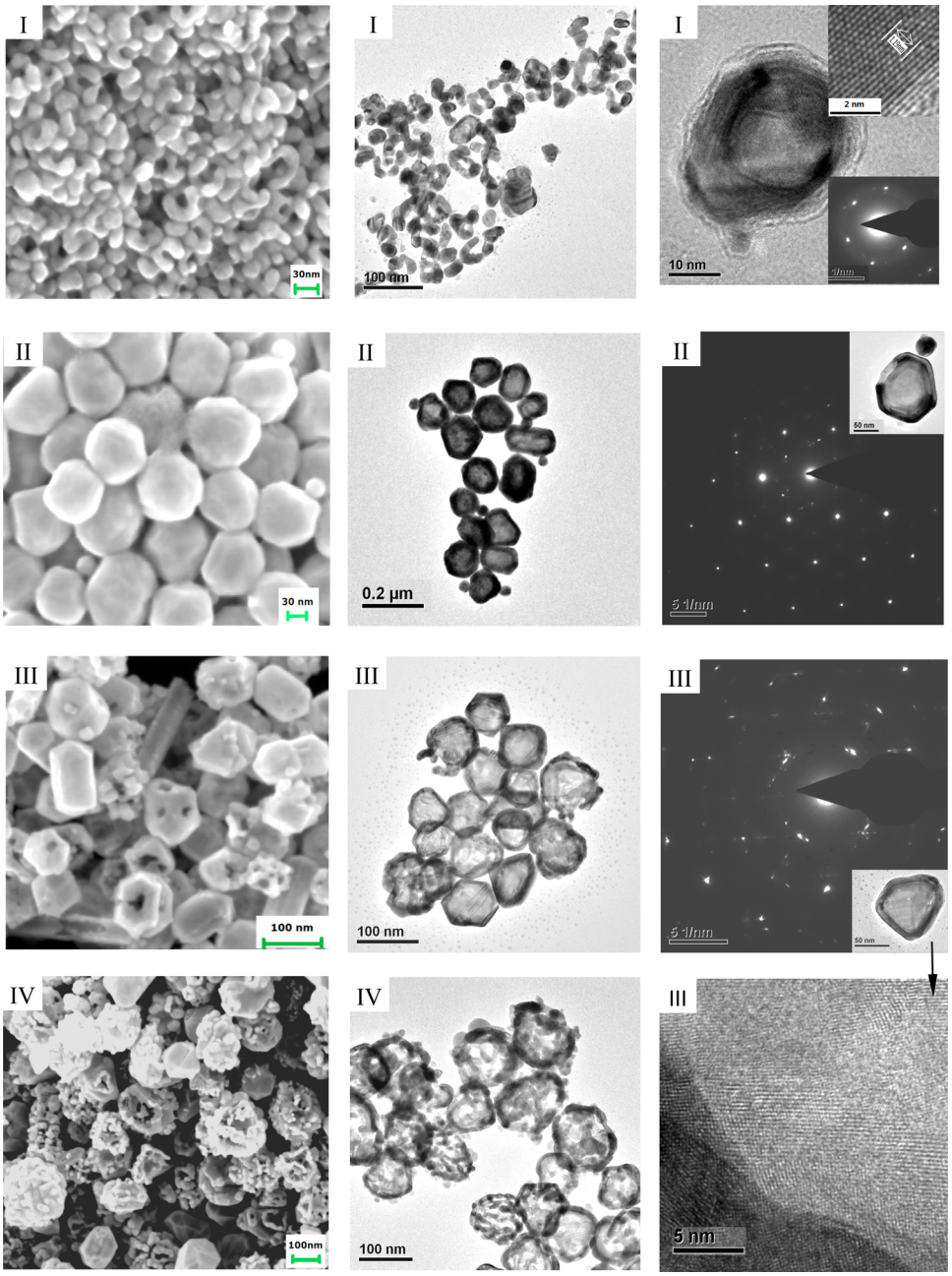


**Figure 2.** TEM, HRTEM, SEM, and SAED images of (I)AuAg540, (II)AuAg600, (III)AuAg696, and (IV) AuAg813. In the HRTEM image of sample I, the total of five lattice spacings is 1.19 nm.

**Table 1. SPR Peak Wavelength and Au/Ag Weight Percentage**

| sample no. | AgAg540 | AuAg600 | AuAg696 | AuAg813 |
|---|---|---|---|---|
| SPR wavelength (nm) | 540 nm | 600 nm | 696 nm | 813 nm |
| Au/Ag (wt %) | 88.5 ± 4.3/ 11.5 ± 0.7 | 71.6 ± 3.6/ 28.4 ± 1.4 | 73.2 ± 3.7/ 26.8 ± 1.4 | 77.3 ± 3.9/ 22.7 ± 1.1 |
| Au:Ag (atomic ratio) | ~5:1 | ~3:2 | ~3:2 | ~3:2 |

the distributions of Au and Ag are identical. From the line-scan EDX, the signals of Au and Ag appear and disappear at the same time at the NP edges and decrease simultaneously within the interior hollow region. With this evidence, we suggest that the Au and Ag atoms form homogeneous solid solution alloys of crystalline structure that are both structurally and chemically stable, with Ag atoms embedded in the Au crystalline lattice. This suggestion is confirmed by atomic-scale HADDF STEM images obtained by the Cs-corrected STEM, shown in Figure 5. From Figure 5a-5e, we observe that AuAg600 forms a perfect single-crystal structure throughout the NPs. The orientation of the outer crystal planes is the (110) facet. SAED patterns also exhibit the typical single-crystal structure. From the EDS results of the partial domain exhibiting a perfect single-crystal lattice, shown in Figure 5g, and the line- or image-mapping in Figure 5h-5l, we confirm that Au and Ag coexist and form a solid-solution alloy. This inference is further supported by the XRD pattern and XPS spectra shown in Figure 6 and Figure 7b respectively, the characteristics of which are further addressed


DOI: 10.1021/acsami.6b03728
ACS Appl. Mater. Interfaces 2016, 8, 16833−16844

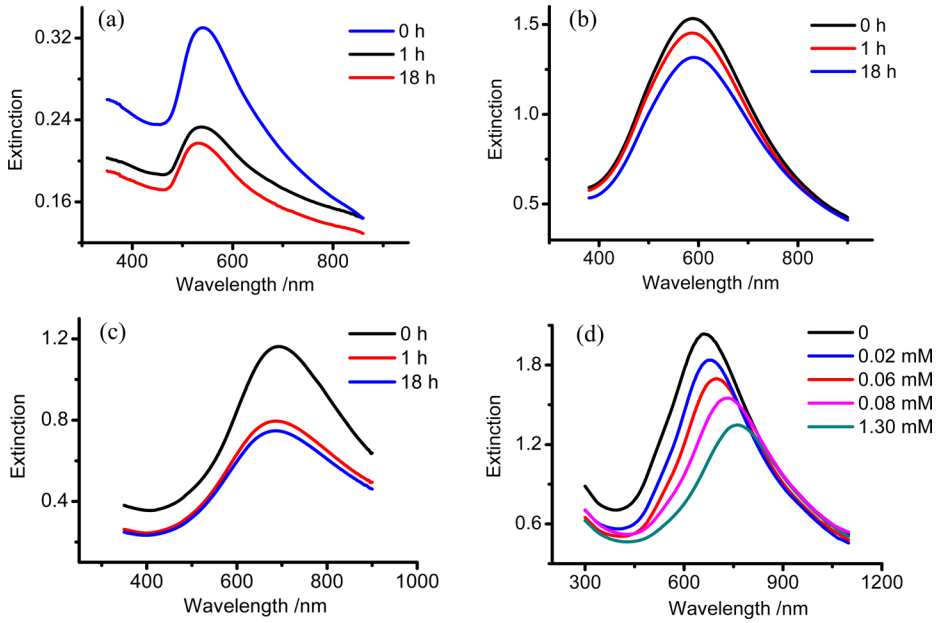


**Figure 3.** UV−vis extinction spectra of (a) AuAg540, (b) AuAg600, and (c) AuAg696 before and after 0, 1, and 18 h of treatment with $H_2O_2$ + $NH_4OH$. (d) Control sample of usual Au−Ag alloyed HPNSs (intermediate state of AuAg813) etched by $H_2O_2$ at different concentrations.

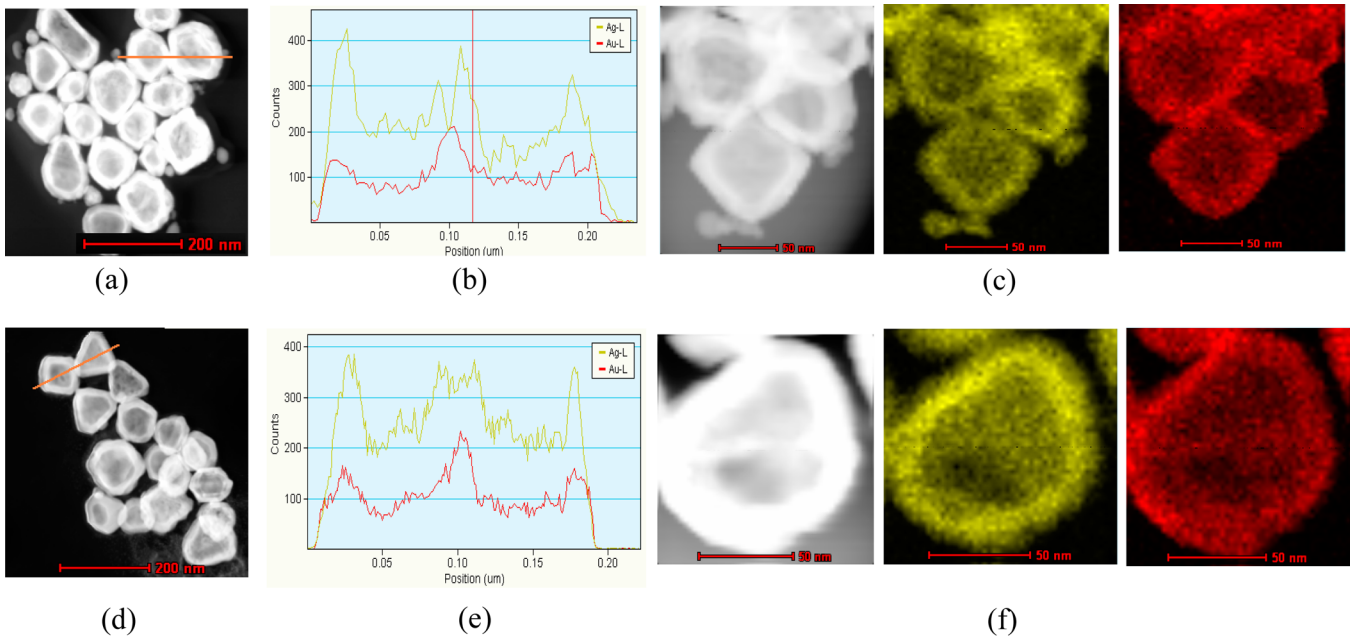


**Figure 4.** STEM and EDS-line and -image mapping (yellow and red representing Ag and Au, respectively) of single-crystal stable hollow Au/Ag alloyed HPNSs of AuAg600 (a−c) before and (d−f) after etching with $H_2O_2$. Weight percentage of Au/Ag is (b) 50.03%/49.96% and (e) 54.39%/45.60%, respectively, according to the EDS line mapping.

in detail later. From the fine analysis of the line-mapping in Figure 5j, although Au and Ag always simultaneously coexist, the relative content of Au and Ag changes from the edge to the interior wall. At the edge domain, the Ag content is relatively lower (Figure S1). This diffusion distribution of Au could be attributed to the formation process.

**AuAg696 NPs.** AuAg696 forms twinned or polycrystalline stable Au−Ag alloyed HPNSs with smooth surfaces, compact walls, and small pinholes on the outer surfaces of most NPs. From the distinct lattice structures shown in the HRTEM images and SAED patterns in Figure 2, single NPs contain twinned or polycrystalline structures. AuAg696 also exhibits good chemical stability similar to that of AuAg600 in corrosion resistance (Figure 3c). The atomic ratio of Au/Ag is ∼3:2. From the very similar XRD pattern and XPS spectra shown in Figure 6 and Figure 7, respectively, we consider that AuAg696 forms Au−Ag solid solution alloys crystalline structures almost identical to those formed by AuAg600.

**AuAg813 NPs.** AuAg813 forms polycrystalline alloyed HPNSs with thin walls and many small flower bud-like protrusions and obvious larger holes on the outer surfaces (Figure 2). The atomic ratio of Au/Ag is also ∼3:2. However, AuAg813 does not exhibit chemical and structural stability. During the galvanic replacement reaction, the SPR peak


DOI: 10.1021/acsami.6b03728
ACS Appl. Mater. Interfaces 2016, 8, 16833−16844

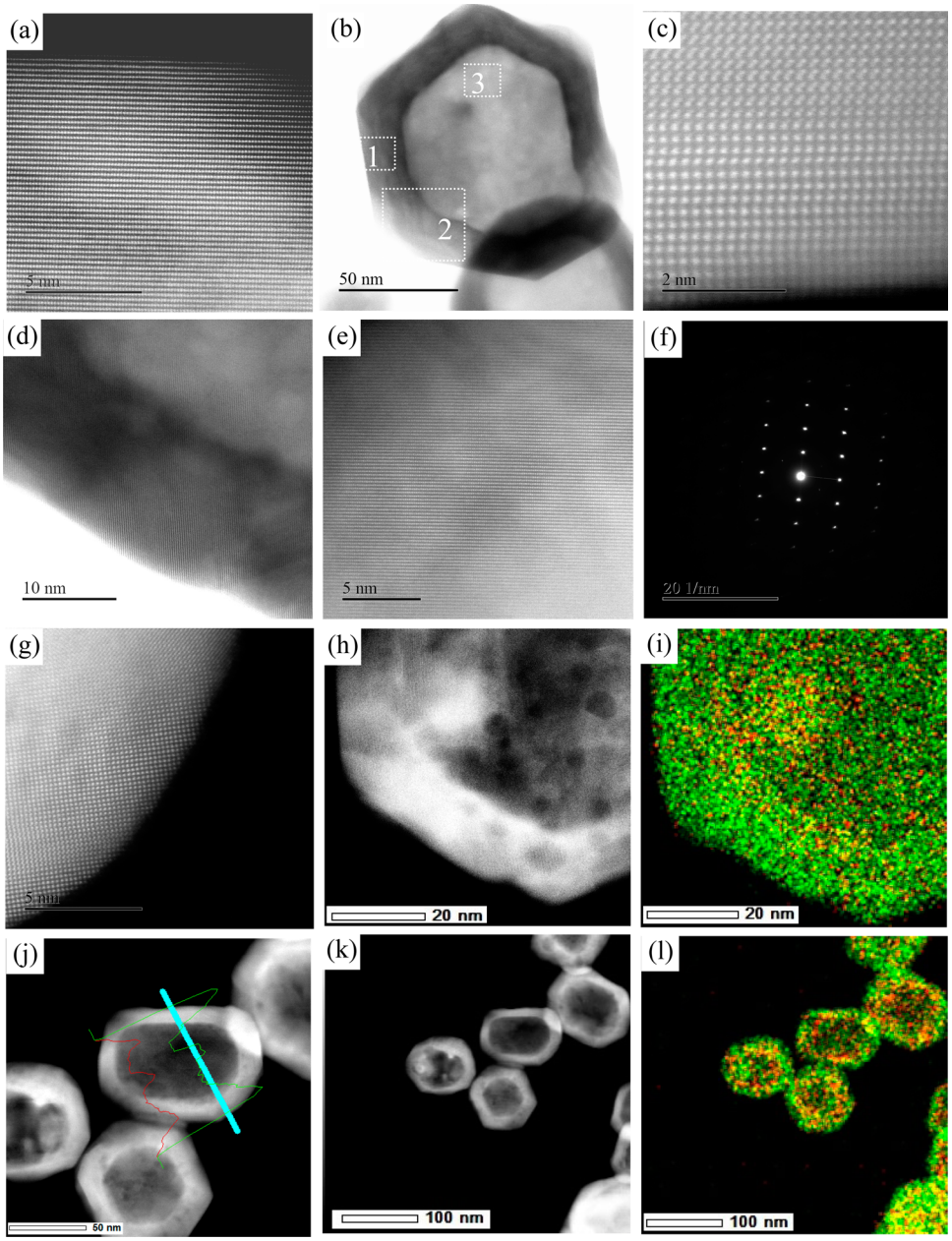


**Figure 5.** Cs-corrected STEM images of Au/Ag600 HPNSs. Panels a, c, d, and e are magnifications of local domains 1, 2, and 3, respectively, of panel b, and panel f is the SAED pattern of single NPs in panel b. (g) Atomic resolution image of the NPs partial edge. The elemental masses of Au and Ag in this domain are 72.4% and 24.6% respectively by EDS measurement. Panels i and l are HADDF STEM image mapping of HPNSs in panels h and k by rapid scanning, respectively; green indicates Au and red indicates Ag. Panel j is a line mapping of single HPNSs, with a green line for Au and a red line for Ag.

wavelength is continuously red-shifted with the addition of $HAuCl_4$, and the morphology and shape also changed continuously at the same time (Figure S2). The Au−Ag alloyed walls became gradually thinner as more holes appeared in the outer surface (Figure 2). While treating the intermediate state of AuAg813 with $H_2O_2$, the SPR peak wavelength is red-shifted. Higher concentrations of $H_2O_2$ lead to greater red-shifting of the SPR peak wavelength, from 662 to 760 nm at $H_2O_2$ concentrations of 0−1.3 mM (Figure 3d). During the etching of $H_2O_2$, the most obvious morphological change is the emergence of small buds on the originally relatively smooth surface; in addition, the overall structure is somewhat loosened (Figure S3). These experimental phenomena and characteristics can be explained by the formation of Au and Ag atoms within AuAg813 HPNSs as random alloys or small nanoclusters aggregates but not as solid solution alloys crystalline structures. In this case, Ag is unstable and easily degraded. This inference is verified by XPS spectral analysis. Distinct variances occur between the spectrum of AuAg813 and those of AuAg540, AuAg600, and AuAg696, indicating that Au and Ag are in different chemical surroundings, despite all being in the zero-valency metallic form with identical binding energy, as shown in Figure 7.[34]

**Analysis of Crystal Structure.** The crystal structures of Ag, Au−Ag alloys, and Au NPs are further characterized by XRD (Figure 6). The patterns of the four Au−Ag alloyed samples predominantly show diffraction peaks characteristic of face-centered cubic (fcc) lattices. Previous works on the powder


DOI: 10.1021/acsami.6b03728
ACS Appl. Mater. Interfaces 2016, 8, 16833−16844

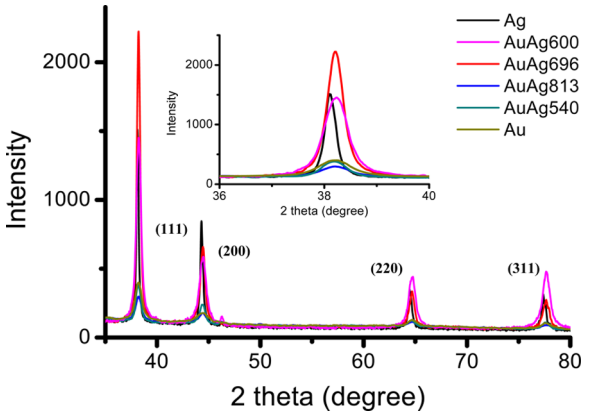


**Figure 6.** XRD spectra of Ag NPs, AuAg600, AuAg696, AuAg813, AuAg540, and Au NPs. Inset: Magnification of the 38.2° peak, assigned to the (111) plane.

XRD spectra of Au−Ag alloyed solid NPs[25,34] reported no obvious differences in the peak locations between Au−Ag alloyed NPs and pure Au or Ag NPs because Au and Ag have very similar lattice parameters of 4.0782 and 4.0862 Å, respectively. However, by fine XRD scanning, the differences among Ag, Au, and Au−Ag alloyed NPs in this work can be observed. For the (111) plane, the diffraction peaks of Ag NPs, AuAg540, AuAg600, AuAg696, AuAg813, and Au NPs are located at 38.10°, 38.24°, 38.22°, 38.22°, 38.20°, and 38.24°, respectively. The peaks of the Au−Ag alloyed NPs are clearly distinct from those of the Ag NPs but are similar to those of the Au NPs. The peak locations are consistent with the data of the (111) planes of ICDD 65-2871 and 65-8424 corresponding to Au and Au−Ag alloyed cubic lattices, respectively. Other planes of (200), (220), and (311) show similar trends (Figure S4). In addition, although the AuAg540 NPs have a crystal lattice structure with a high degree of crystallization, other factors such as the much smaller size, the multicrystalline structure could greatly affect the diffraction intensity. Meanwhile, the AuAg813 NPs have multicrystalline structures; the XRD spectra of AuAg600 and AuAg696 exhibit significantly stronger diffraction intensities than those of AuAg540 and AuAg813, demonstrating that AuAg600 and AuAg696 contain more highly crystallized alloyed structures.

XPS is used to examine the valence states of Au and Ag after the galvanic replacement reaction is completed. The peaks at ∼368 and ∼374 eV can be assigned to the Ag $3d^{5/2}$ and $3d^{3/2}$ of metallic Ag, respectively, while those at 83.7 and 87.4 eV can be assigned to the Au $4f^{7/2}$ and $4f^{5/2}$ of metallic Au, respectively.[36] According to the results (Figure 7, Figure S5), for the AuAg600, AuAg696 HPNSs and AuAg540 solid NPs, the peaks of Au $4f^{7/2}$ appear approximately identical, locate at 83.94, 83.91, and 83.91 eV, which is lower in energy than the corresponding peak of 84.51 eV for AuAg813 HPNSs. Similarly, the peaks of Ag $3d^{5/2}$ for AuAg600, AuAg696, and AuAg540 are very similar at 367.87, 367.51, and 367.81 eV respectively, and lower in energy than the 368.41 eV peak of AuAg813 HPNSs. The measurement error of XPS is ∼0.2 eV, so the obvious variances in XPS peak locations illustrate that the chemical environments of the Au and Ag atoms within AuAg540, AuAg600, AuAg696, and AuAg813 are distinctly different.

According to XRD and XPS results, combining the apparent difference in structural and chemical stability, we speculate that Ag atoms entered the lattice of ordered Au atoms to form Au−Ag solid solution alloys crystalline structures in AuAg600 and AuAg696. This speculation is supported by the binding energies of Ag−Au and Au−Au, which shows similar trends with changes in atomic distance.[35] In AuAg600 and AuAg696, Ag has high chemical stability and is not degradable. However, for AuAg813, Ag is unstable; we attribute this to the formation of Au and Ag nanocluster aggregates, rather than solid solution alloys throughout a given NP.

**Influence of the Sacrificial Ag NPs' Size.** Clearly the size of the sacrificial Ag NPs can significantly affect the morphology, crystalline structure, and stability of Au−Ag alloyed HPNSs. Determining the accurate amount of Ag before and after the galvanic replacement reaction may elucidate the mechanism. Taking AuAg696 as an example, the average size of the sacrificial Ag NPs is 64.30 nm by dynamic light scattering (DLS) measurements (Figures 8a and S6a). After the galvanic replacement reaction, the most frequent size of Ag particles within AuAg696 HPNSs is 63.14 nm by single-particle ICP-MS measurement (Figures 8b and S6b).

Considering the measurement error, these two values of the Ag NP sizes illustrate that Ag does not lose significant mass and is almost totally fused into the Au−Ag alloyed walls of the HPNSs. According to the mechanistic illustration of the galvanic replacement reaction between $HAuCl_4$ and Ag NPs,[16] the Ag nanostructures were continuously dissolved and the resultant elemental Au was epitaxially deposited on the surface of each Ag NP template simultaneously, for the fast interdiffusion of Au and Ag at 100 °C, the Au layer was transformed into an Au−Ag alloy. Possibly because of this, it is found that the diameter of the hollow core of the HPNSs formed in this study is approximately equal to the size of the sacrificial Ag NPs. For the example of AuAg696, the average size of the hollow core is 63.90 nm, approximately equal to the DLS diameter of the sacrificial Ag NPs. A representative TEM image for the size measurements and the size distribution of hollow cores are shown in Figure S7. From TEM images, the wall thickness is ∼10 nm and the distributions of Au and Ag atoms within the walls are homogeneous (Figure 4). However, the degree of compactness in the walls remains unclear.

We consider that this may directly correlate with the size of the sacrificial Ag NPs, as schematically illustrated in Figure 9. Given the radius r of Ag NPs and the radius R of HPNSs, in order to obtain compact Au−Ag alloyed walls, the wall thickness should be no less than 10 nm, and the volume of walls should not be smaller than the volume of Ag NPs, because Ag atoms are homogeneously distributed within the Au−Ag alloyed walls. Namely, $R$ and $r$ must meet the limitations $R - r \geq 10$ nm, and $4/3\pi (R^3 - r^3) \geq 4/3\pi r^3$. By calculating, $r$ should be less than or equal to 38 nm; when the diameter of Ag NPs is less than 76 nm, during the process of galvanic replacement reaction, the amount of Ag is sufficient for the Au−Ag alloy to form compact Au−Ag solid-solution alloyed crystalline walls.

**Evaluation of HPNSs' Catalytic Performance.** To further investigate the properties of the solid solution alloys crystalline structures, the catalytic activities of the four Au−Ag alloyed NPs are evaluated with the reduction conversion of *p*-nitrophenol to *p*-aminophenol in the presence of $NaBH_4$. After addition of a freshly prepared aqueous solution of $NaBH_4$, the peak corresponding to 4-nitrophenol was immediately red-shifted from 317 to 400 nm because of the formation of 4-nitrophenolate ions in the alkaline condition caused by the addition of $NaBH_4$. In the absence of proper catalyst, the


DOI: 10.1021/acsami.6b03728
ACS Appl. Mater. Interfaces 2016, 8, 16833−16844

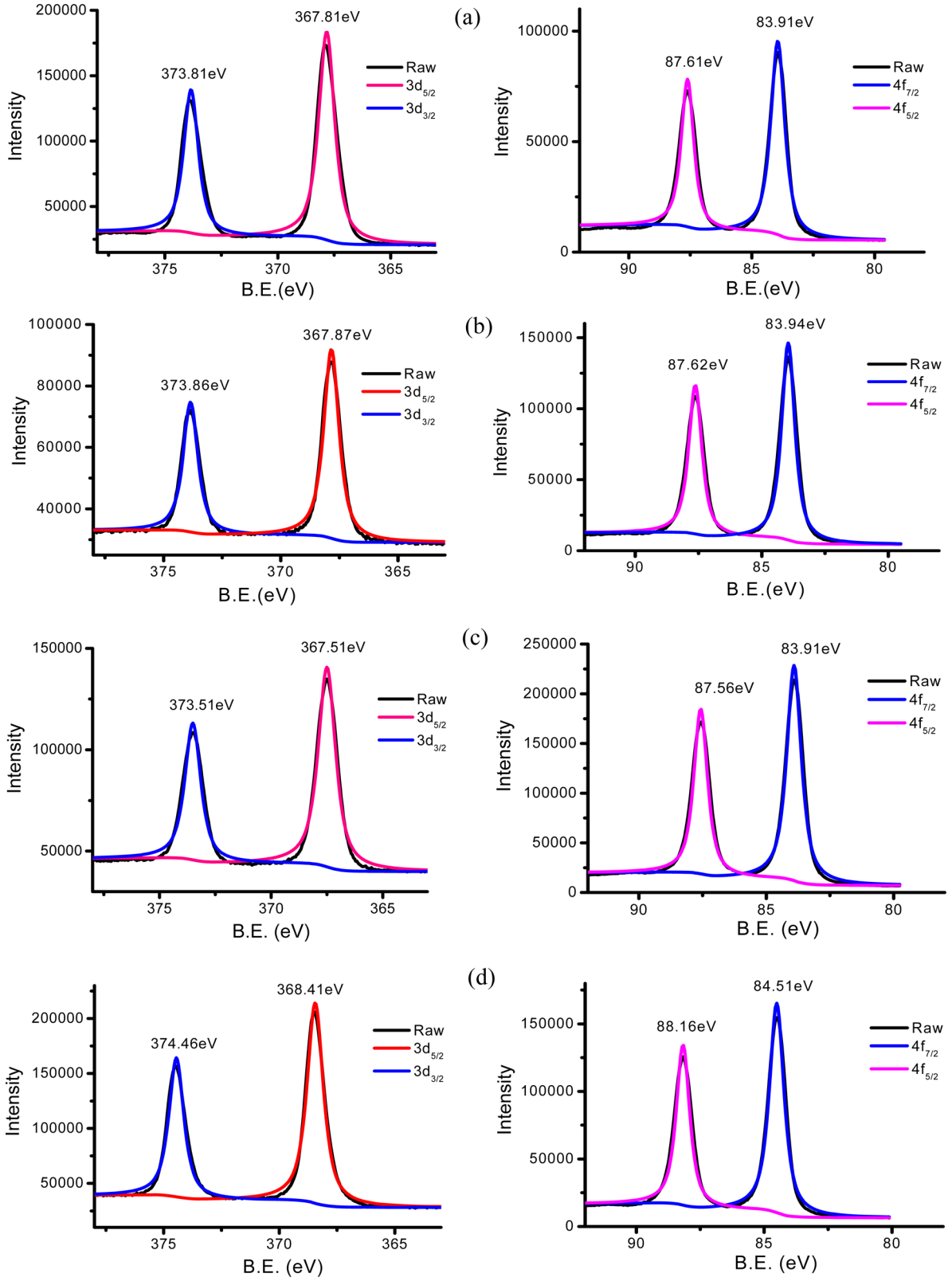


**Figure 7.** XPS spectra of Au−Ag alloyed NPs' Ag 3d and Au 4f orbitals, respectively, of (a) AuAg540, (b) AuAg600, (c) AuAg696, and (d) AuAg813 recorded from dried powder. B.E.: binding energy.

thermodynamically favorable reduction of 4-nitrophenol was not observed. The standard reduction potentials for 4-nitrophenol/4-aminophenol and $H_3BO_3/BH_4-$ are 0.76 and 1.33 V, respectively. The peak indicating 4-nitrophenol ions at 400 nm remained unaltered over multiple days.[34]

At ambient conditions, the reduction reaction of 4-nitrophenol to 4-aminophenol is a common practice for checking the catalytic activity of unsupported Au NPs.[25] Figure 10a shows the UV−vis absorption spectra of the 4-nitrophenol ion and 4-aminophenol, and Figure 10b shows representative



DOI: 10.1021/acsami.6b03728
ACS Appl. Mater. Interfaces 2016, 8, 16833−16844

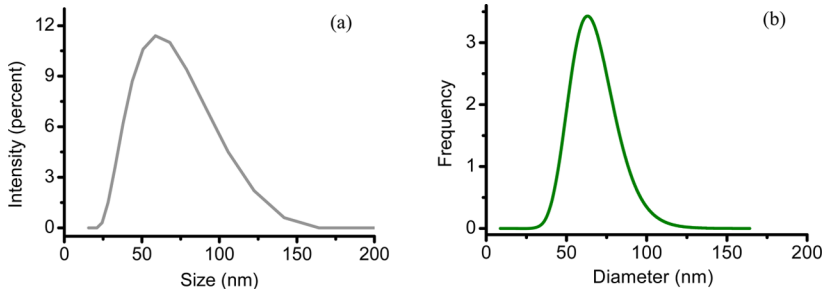


**Figure 8.** (a) Size distributions of sacrificial Ag NPs for AuAg696 as measured by DLS; peak is located at 64.30 nm. (b) Ag particles counted as a function of diameter measured by SP-ICP-MS; peak is located at 63.14 nm.

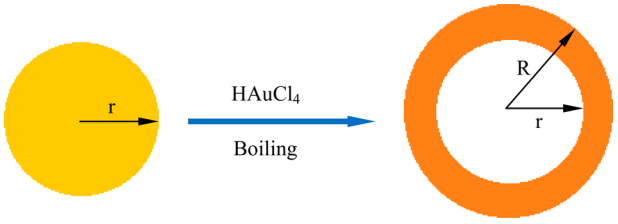


**Figure 9.** Illustration of size changes during aqueous synthesis of Au–Ag alloyed HPNSs with compact walls of solid-solution alloyed crystalline structure by galvanic replacement reaction.

successive UV–vis absorption spectra of the catalytic reduction of 4-nitrophenol into 4-aminophenol. As shown in Figure 10b, the UV–vis absorption wavelength is immediately red-shifted from the 317 nm peak of 4-nitrophenol to the 400 nm peak of 4-nitrophenol ion upon the addition of $NaBH_4$ into the 4-nitrophenol solution in the presence of AuAg696 alloyed HPNSs as catalysts. Subsequently, a successive decrease in the peak height at 400 nm and the gradual development of a new peak at 300 nm indicates the formation of 4-aminopehnol, corresponding to changes in the solution color from bright yellow to light yellow to colorless. The wavelength of the product is consistent with that of pure 4-aminophenol (Figure 10a).

**Catalytic Activity.** The rapid catalytic conversions of 4-nitrophenol to 4-aminophenol in the presence of the Au–Ag alloyed NPs were quantitatively monitored. Similar spectral changes were also obtained for the other three alloyed samples. In the contrast experiments on pure Au and Ag NPs, the results showed that no obvious catalytic effects were observed in the pure Au and Ag NP systems under the conditions of equal Au and Ag element quantities, respectively (Figure S8). In this catalytic experiment, the concentration of $BH_4^-$, used as a reductant, largely exceeds that of 4-nitrophenol; thus, the reduction rate is considered independent of the concentration of $NaBH_4$ and the kinetic process of the reaction can be easily studied by simply monitoring the change in intensity of the 400 nm absorption peak correlated with the concentration of *p*-nitrophenol over time. Although a previous study reported that citrate could directly reduce *p*-nitrophenol and significantly enhance the initial rate of the reaction,[29] in our experiments, the sacrificial Ag NPs with citrate surfactant ligands had been centrifuged and redispersed. The residual citrate was too dilute to cause detectable effects, which was further confirmed by the lack of observed catalytic activity in the pure Ag NPs; therefore, the effect of the citrate on the catalysis should be negligible. Once the $NaBH_4$ is added, the Au–Ag alloyed NPs immediately catalyze the reaction by relaying electrons from the donor $BH_4^-$ to the acceptor 4-nitrophenol as soon as both are adsorbed onto the particle surfaces. From previous works,[34] the catalytic reduction reaction from 4-nitrophenol to 4-aminophenol occurs with pseudo-first-order kinetics. The apparent rate constant can be obtained from the decrease in peak intensity at 400 nm over time. Figure 11 shows the plot of $\ln(A_t/A_0)$ against reaction time for all four Au–Ag alloyed NPs as catalysts. Each species shows a good linear fitting of $\ln(A_t/A_0)$ versus reaction time. The apparent rate constants of AuAg540, AuAg813, AuAg600, and AuAg696 are $1.2 \times 10^{-2}$, $0.9 \times 10^{-2}$, $1.1 \times 10^{-2}$, and $3.2 \times 10^{-2}$ $s^{-1}$ at 25 °C, respectively. The reaction rate of AuAg696 is significantly higher than those of the other three samples, and the rate constants of AuAg540 and AuAg600 are very similar and somewhat higher than that of AuAg813. The reaction parameters, including the concentrations of Au, 4-nitrophenol, and $NaBH_4$, were consistent for each Au–Ag alloyed sample, so the apparent rate constant depended on the physicochemical properties of the Au–Ag alloyed NPs.

According to the characteristic results, AuAg600 and AuAg696 form alloyed crystalline HPNSs with chemical and

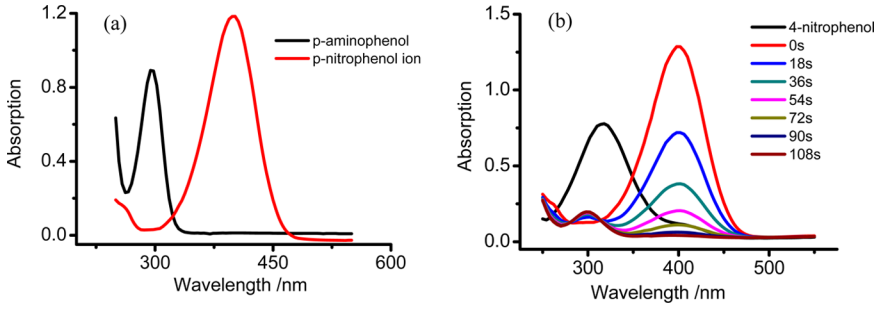


**Figure 10.** (a) UV–vis absorption spectra of *p*-nitrophenol ion and *p*-aminophenol and (b) successive UV–vis absorption spectra taken before (black line) and after adding $NaBH_4$ to 4-nitrophenol solution in the presence of AuAg696 alloyed HPNSs.


DOI: 10.1021/acsami.6b03728
ACS Appl. Mater. Interfaces 2016, 8, 16833–16844

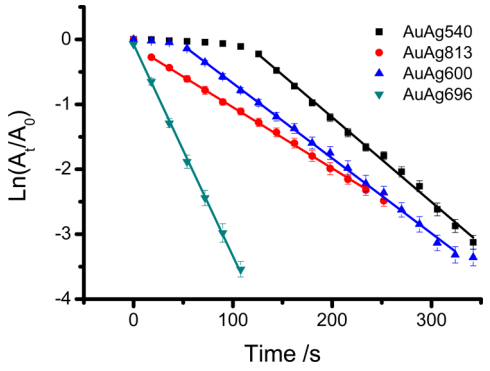


**Figure 11.** Plot of $\ln(A_t/A_0)$ against catalytic reaction times for all alloyed nanostructures.

structural stability, AuAg540 is solid Au−Ag alloyed NPs without Ag degradation, and AuAg813 is multicrystalline Au−Ag alloyed HPNSs with surface holes and Ag degradation. From previous reports, chemically stable Au−Ag alloyed NPs exhibited higher catalytic abilities with increasing Au weight percentages.[25] Chemically unstable Au−Ag alloyed HPNSs, as judged by the etching of $H_2O_2$, exhibited higher catalytic ability after the structures became more open.[16,29] It may be more easily understood that the increase of Au weight percentage and openness of the morphology could distinctly accelerate the catalytic reaction rate by the experiments performed in this work. AuAg696 exhibited a significantly higher reaction rate than solid AuAg540 NPs or compact solid-walled AuAg600 HPNSs. In addition, although AuAg540 is smaller in size with a higher specific area, AuAg600 presented a rate somewhat higher

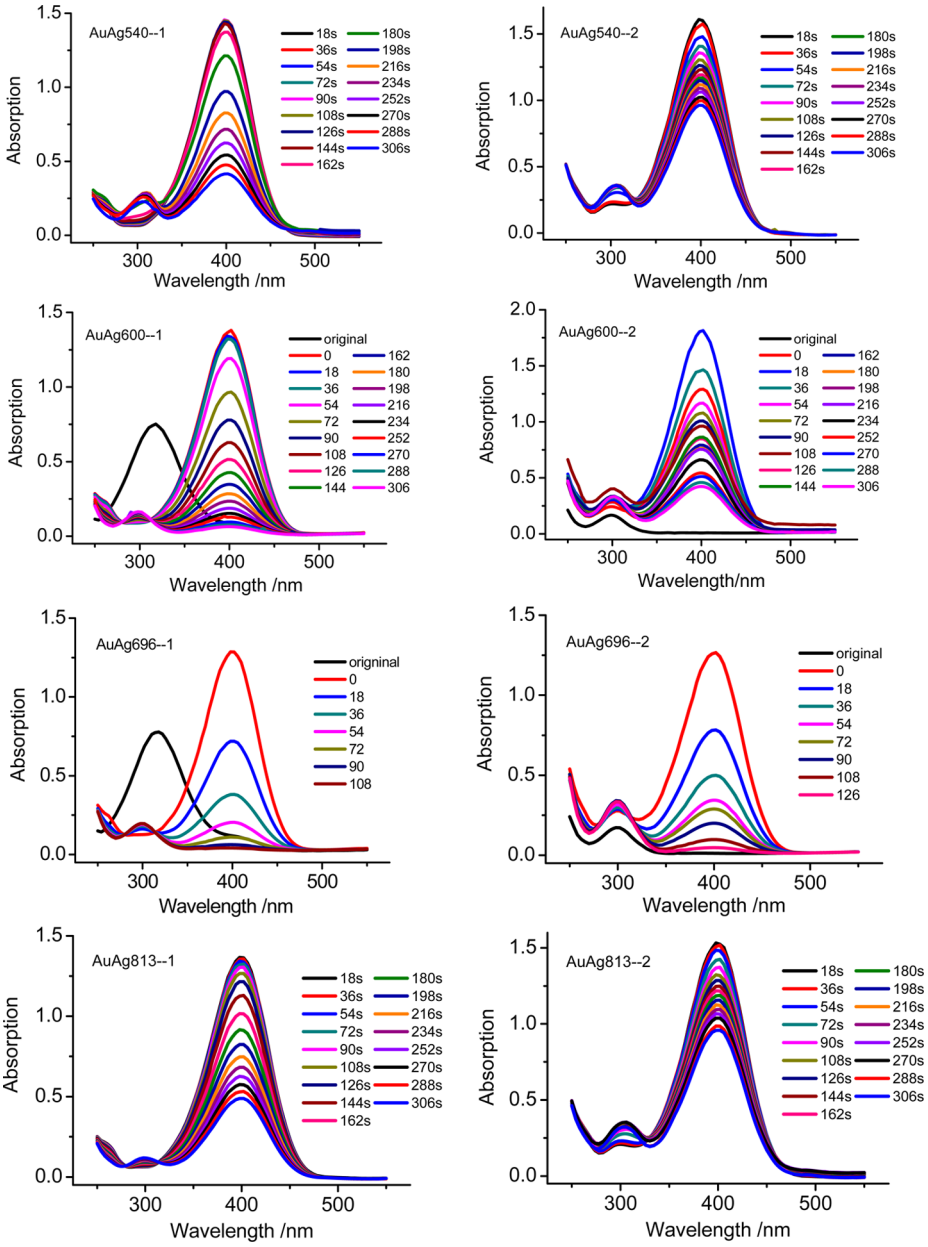


**Figure 12.** Successive UV−vis absorption spectra of AuAg540, AuAg600, AuAg696, and AuAg813 Au−Ag alloyed NPs before and after cyclic use. For AuAg696, AuAg696-1 is the spectrum versus time for the first reaction, and AuAg696-2 is that for the second reaction. Black lines labeled as "original" exhibit initial spectra of reaction solution before the addition of $NaBH_4$.



DOI: 10.1021/acsami.6b03728
ACS Appl. Mater. Interfaces 2016, 8, 16833−16844

than AuAg540 did, which may be attributed to the outer crystalline surface of {110} facets with higher surface energy. For various fcc crystalline planes, the change in surface energy obeys the order of $\gamma\{111\} < \gamma\{100\} < \gamma\{110\}$.[36] AuAg696 with small pinholes within the Au−Ag alloyed wall provides many more active sites for the reduction reaction. However, AuAg813, with the most open morphology, exhibited a significantly lower rate relative to AuAg696, which indicates that for reaction systems with equal Au contents the Au−Ag alloyed crystalline structure is as important for catalytic ability as morphology. In fact, crystallinity may be more important than morphology in determining the catalytic ability, because the reaction rate of AuAg813 was somewhat lower than that of AuAg540. The above analysis and comparison of reaction rates is based on statistical data after the catalysis of the reduction reactions. Reactivity platforms are present for AuAg540 and AuAg600 before the beginning of the catalytic reaction, reflecting the insufficient number of active sites at the beginning to initiate the reaction on solid NPs or compact walls without pinholes, so these materials require longer activation periods. However, AuAg696 and AuAg813 have more open morphologies and the catalytic reactions began immediately after the addition of $NaBH_4$.

**Cyclic Usage Efficiency.** In addition to the variance in catalytic reaction rate, the cyclic usage efficiencies of the four Au−Ag alloyed samples also exhibited distinct differences. Once the reaction solution became colorless and the absorption peak at 400 nm reached an intensity of zero, 30 $\mu$L of 7.5 mM 4-nitrophenol and 100 $\mu$L of 1.0 M $NaBH_4$ were successively added. The successive UV−vis absorption spectra were recorded to evaluate the cyclic usage efficiency of the four kinds of Au−Ag alloyed samples, as shown in Figure 12. In the second reactions, AuAg813 and AuAg540 presented very similar catalytic abilities, with ∼40% transfer efficiency after 306 s and much slower reaction rates than those displayed in the first reaction. The transfer efficiency of AuAg600 was ∼80% after 306 s, with no platform period. For AuAg696, the transfer efficiency was ∼96% after 126 s, only somewhat slower than the rate of the first reaction. After five cyclic uses, the transfer efficiency of AuAg696 remained as high as 77.58% after 306 s (Figure S9). The morphology of the AuAg696 HNPSs did change slightly after five cycles; small bumps were observed on the surfaces of some AuAg696 HPNSs, as shown in high-resolution SEM images (Figure S10). These features probably result from the migration and rearrangement of Au or Ag atoms on the particle surfaces during the catalytic reaction.

**Key Factors of Catalytic Performance.** It can be speculated that the open morphology and alloyed crystalline structure, corresponding to chemical and structural stability, are the two crucial factors in determining the catalytic abilities of Au−Ag alloyed NPs. The morphological effect is obvious in enhancing catalytic activity, because openness corresponds to larger specific surface areas, more active sites, and more space for quicker diffusion of reactants and resultants. The influence of the atomic-scale microstructure or the arrangement of bimetallic atoms on catalytic performance is less clear. However, very recent reports[37,38] have provided a reasonable explanation: "making gold catalytically active requires atomically dispersed atoms rather than larger nanoparticles." For the samples of AuAg600 and AuAg696 in this work, Ag is assumed to have entered the Au crystal lattice to form bimetallic alloyed microstructures, based on the bimetallic homogeneous distribution and the chemical and structural stability of the products. For the sample of AuAg813, the Au and Ag atoms formed random alloying microstructures or nanocluster aggregates without chemical stability. From the analysis above, we can understand that, although AuAg813 had a more open morphology than AuAg696, AuAg696 exhibited significantly better catalytic performance, because the Au atoms were better dispersed for the existence of ordered arrangement of Ag atoms. Another possibility is that the coordination number of AuAg696 was the most suitable, so the binding of reaction intermediates to the surfaces was neither too strong nor too weak, leading to the highest catalytic performance.

## CONCLUSION

Four kinds of Au−Ag alloyed NPs with different morphologies and subnanoscale crystalline structures were synthesized by adjusting the size of the sacrificial Ag NPs used in the galvanic replacement reaction. The Ag contents experienced little loss and remained similar before and after the galvanic replacement reaction for single chemically and structurally stable NPs, which illustrated the effect of Ag NP size on the morphology of Au−Ag alloyed HPNSs. When the diameter of the Ag NPs was less than the critical value of 76 nm, obtained by simple theoretically analysis and calculation, the alloyed HPNSs formed solid solution alloys crystalline structures with high chemical and structural stability having compact and pinhole-free Au−Ag alloyed walls. With the increase of the sacrificial Ag NP size, small pinholes appeared within the Au−Ag alloyed walls and opened the morphology of the nanostructures. The crystalline structure maintained an alloy state and the nanostructures retained chemical and structural stability. For sacrificial Ag NPs larger than ∼80 nm, the resultant Au−Ag alloyed HPNSs formed random alloyed structures containing many nanocluster aggregates with much larger holes and small protrusions from the Au−Ag alloyed walls. In these HPNSs, Ag was easily degradable by $H_2O_2$ and the apparent structure changed with etching.

The atomic crystalline structure of Au−Ag bimetallic NPs is much more significant than morphology in determining the catalytic ability of the nanostructures for the catalytic reduction of *p*-nitrophenol by $NaBH_4$ to afford *p*-aminophenol. The Au−Ag alloyed HPNSs with better surface crystalline alloying microstructures and open morphologies presented much higher catalytic reaction rates and better cyclic usage efficiencies. This is because the effective alloyed crystalline microstructure surfaces provide better dispersions of the active Au atoms, which contribute to the higher catalytic activities of the structures.

The as-synthesized Au−Ag alloyed HPNSs proposed here have a facile preparation, stable physicochemical properties without Ag degradation, and good catalytic performance with short reaction times. The findings provide new information toward understanding the effects of Au−Ag alloy hollow nanostructures on the catalytic activity for the reaction producing *p*-aminophenol from p-nitrophenol.

## METHODS

**Reagents.** Analytical-grade trisodium citrate ($Na_3Ct$), $NH_4OH$, and $NaBH_4$ were obtained from Sigma-Aldrich, while $AgNO_3$ was obtained from Alfa-Aesar and used without further purification. $HAuCl_4{\cdot}4H_2O$ was purchased from Beijing Chemical Reagent Company and $H_2O_2$, p-nitrophenol, and *p*-aminophenol were purchased from Beijing Chemical Factory and used as received. All


DOI: 10.1021/acsami.6b03728
ACS Appl. Mater. Interfaces 2016, 8, 16833−16844

aqueous solutions were prepared using deionized (DI) water with a resistivity of 18.2 MΩ·cm.

**Synthetic Procedures.** The Au−Ag alloyed NPs were synthesized by a $HAuCl_4$ galvanic replacement reaction of Ag NPs. Small Ag seeds were first synthesized by the $NaBH_4$ and $Na_3Ct$ coreduction of $AgNO_3$, based on existing protocols;[39] larger Ag NPs of different sizes were obtained by the successive seed-growth method.

In a typical synthesis, a 150 mL round-bottom flask was washed with $HNO_3$ + 3HCl (aqua regia) and DI water, and then 20 mL of 1.0 wt % aqueous $Na_3Ct$ and 75 mL DI water were placed in the flask and heated to 70 °C. Next, 1.7 mL of 1.0 wt % aqueous $AgNO_3$ and 2.0 mL of 0.1 wt % aqueous $NaBH_4$ were quickly added to the flask with vigorous stirring. After 1 h, the solution was cooled to room temperature under ambient conditions. The product was bright yellow and collected by centrifugation. The solution of Ag seeds was redispersed with an equal volume of DI water. Then 10 mL of the obtained Ag seeds and 1.7 mL of 1.0 wt % aqueous $AgNO_3$ were quickly added with mild stirring to a solution of 2.0 mL of 1.0 wt % aqueous $Na_3Ct$ and 75 mL DI water at the boiling temperature of the solution. The solution was boiled for 1 h, after which it was cooled to room temperature, where upon the products were centrifuged and redispersed.

Four kinds of Au−Ag alloyed NPs were synthesized,[16] referred to as AuAg540, AuAg600, AuAg696, and AuAg813 according to the wavelengths of the SPR peaks from the products. Taking AuAg600 as an example, a certain volume of Ag NPs with diameters of ∼60−70 nm was added into a round-bottom flask and heated with stirring. After the mixture was boiled, three doses of 100 μL of 1.0-mM aqueous $HAuCl_4$ were added subsequently. The color of the solution changed from bright yellow to white, then to brown-yellow, and maintained this color as more $HAuCl_4$ was added. AuAg696 and AuAg813 were synthesized using sacrificial Ag NPs of ∼70−80 and ∼80−90 nm, respectively. AuAg514 also used sacrificial Ag NPs of ∼70−80 nm, but the amount of $HAuCl_4$ in the third dose was 300 μL rather than 100 μL and the color of the sample was dark purple.

**Characterization.** UV−visible (UV−vis) extinction spectra of the samples were recorded using PerkinElmer Lambda650 UV−vis spectrometers, and the curves of extinction coefficients versus time and the catalytic kinetic reaction processes with p-nitrophenol were obtained using VARIAN Cray50 Scan UV−vis spectrometers. Transmission electron microscopy (TEM), high-resolution TEM (HRTEM), high-angle annular dark field scanning transmission electron microscopy (HAADF-STEM), selected-area electron diffraction (SAED), and energy-dispersive X-ray spectrum (EDS) and mapping images were recorded by an FEI Tecnai F20 TEM with an accelerating voltage of 200 kV, equipped with an EDS analyzer, and a JEM ARM200F spherical aberration-corrected STEM (Cs-corrected STEM). The TEM samples were prepared by placing drops of the final product on superthin C-coated Cu grids and drying the samples under ambient conditions. Scanning electron microscopy (SEM) images were recorded by ZEISS Merlin SEM apparatus. Room-temperature X-ray diffraction (XRD) patterns were recorded using a Rigaku D/MAX TTRIII (CBO) diffractometer in the scan region of 30−85° at a rate of 8°/min and step size of 0.02°. X-ray photoelectron spectroscopy (XPS) data was recorded using an ESCALAB 250Xi XPS apparatus, while a precise quantitative analysis of the Au and Ag elements within the alloyed HPNSs and single-particle inductively coupled plasma mass spectroscopy (ICP-MS) analysis of the alloyed NPs were recorded using a PerkinElmer NexION 300X mass spectrometer.

The catalytic reduction reactions of 4-nitrophenol using the four kinds of Au−Ag alloyed NPs as catalysts were compared. The concentration of Au was set equal to 0.1 mM in the catalysis solution, as determined by ICP-MS. In a typical reduction reaction, 30 μL of 7.5-mM 4-nitrophenol and 100 μL of 0.1-mM catalysis solution were mixed with 2.5 mL of highly purified water at 25 °C in a quartz cell. A freshly prepared aqueous solution of 100 μL of 1.0-M $NaBH_4$ was added and mixed uniformly. UV−vis absorption spectra were recorded over time to monitor changes in the reaction mixture.

## ■ ASSOCIATED CONTENT

### Supporting Information

The Supporting Information is available free of charge on the ACS Publications website at DOI: 10.1021/acsami.6b03728.

The element mass percent of Au and Ag at different sampling position along the track of line mapping for a whole HPNSs of AuAg600; TEM images of Ag NPs as sacrifices and morphology change of the intermediate state of AuAg813; XRD spectra of samples assigned to (200), (220), and (311) plane; XPS spectra of alloyed samples; size distribution of sacrificial Ag NPs and Ag contents in AuAg696 HNPSs; morphology and successive UV−vis absorption spectra of pure Au and Ag NPs as contrast for the catalytic reaction; representative TEM image and statistical size distribution of hollow cores of AuAg696; successive spectra of AuAg696 during the fifth cycle; morphology characteristics of AuAg696 HPNSs before and after five cyclic usages (PDF)

## ■ AUTHOR INFORMATION


### Corresponding Authors

*E-mail: liurx@nanoctr.cn. Phone:+86-10-82545927. Fax:+86-10-62656765.
*E-mail: pjiang@nanoctr.cn.
*E-mail: gegl@nanoctr.cn.

### Author Contributions

§These authors contributed equally.


### Notes

The authors declare no competing financial interest.

## ■ ACKNOWLEDGMENTS

This work was supported by the Beijing Natural Science Foundation (No. 2143042), the National Natural Science Foundation of China (No.51303037), and National Key Scientific Instrument and Equipment Development Projects of China (No.2014YQ090709). Many thanks to the valuable discussion of Prof. Meng He (NCNST) regarding XRD spectrum, and thanks for the help of Engineer Peng Xu (NCNST) on XPS measurements.

## ■ ABBREVIATIONS

NPs, nanoparticles
HPNSs, hollow and porous nanoshell structures
UV−vis, ultraviolet−visible
TEM, transmission electron microscopy
HRTEM, high-resolution TEM
HAADF-STEM, high-angle annular dark field scanning transmission electron microscopy
SAED, selected-area electron diffraction
SEM, scanning electron microscopy
EDS, energy-dispersive X-ray spectrum
Cs-corrected STEM, spherical aberration-corrected STEM
XRD, X-ray diffraction
XPS, X-ray photoelectron spectroscopy
ICP-MS, inductively coupled plasma mass spectroscopy

## ■ REFERENCES

(1) Alloyeau, D.; Mottet, C.; Ricolleau, C. *Nanoalloys: Synthesis, Structure and Properties*; Springer: Berlin, 2012.
(2) Calvo, F. *Nanoalloys: From Fundamentals to Emergent Applications*; Elsevier Science: Amsterdam, 2013.


DOI: 10.1021/acsami.6b03728
ACS Appl. Mater. Interfaces 2016, 8, 16833−16844

(3) Ferrando, R.; Jellinek, J.; Johnston, R. L. Nanoalloys: From Theory to Applications of Alloy Clusters and Nanoparticles. *Chem. Rev.* **2008**, *108*, 845−910.
(4) You, H.; Yang, S.; Ding, B.; Yang, H. Synthesis of Colloidal Metal and Metal Alloy Nanoparticles for Electrochemical Energy Applications. *Chem. Soc. Rev.* **2013**, *42*, 2880−2904.
(5) Holewinski, A.; Idrobo, J.-C.; Linic, S. High-Performance Ag-Co Alloy Catalysts for Electrochemical Oxygen Reduction. *Nat. Chem.* **2014**, *6*, 828−834.
(6) Zhao, Y.; Ye, C.; Liu, W.; Chen, R.; Jiang, X. Tuning the Composition of AuPt Bimetallic Nanoparticles for Antibacterial Application. *Angew. Chem., Int. Ed.* **2014**, *53*, 8127−8131.
(7) Sheldon, M. T.; Van de Groep, J.; Brown, A. M.; Polman, A.; Atwater, H. A. Plasmoelectric Potentials in Metal Nanostructures. *Science* **2014**, *346*, 828−831.
(8) Sharma, M.; Pudasaini, P. R.; Ruiz-Zepeda, F.; Vinogradova, E.; Ayon, A. A. Plasmonic Effects of Au/Ag Bimetallic Multispiked Nanoparticles for Photovoltaic Applications. *ACS Appl. Mater. Interfaces* **2014**, *6*, 15472−15479.
(9) Larguinho, M.; Baptista, P. V. Gold and Silver Nanoparticles for Clinical Diagnostics − from Genomics TO Proteomics. *J. Proteomics* **2012**, *75*, 2811−2823.
(10) Gao, C.; Hu, Y.; Wang, M.; Chi, M.; Yin, Y. Fully Alloyed Ag/Au Nanospheres: Combining the Plasmonic Property of Ag with the Stability of Au. *J. Am. Chem. Soc.* **2014**, *136*, 7474−7479.
(11) Liu, H.-L.; Nosheen, F.; Wang, X. Noble Metal Alloy Complex Nanostructures: Controllable Synthesis and Their Electrochemical Property. *Chem. Soc. Rev.* **2015**, *44*, 3056.
(12) Liu, S.; Chen, G. Y.; Prasad, P. N.; Swihart, M. T. Synthesis of Monodisperse Au, Ag, and Au-Ag Alloy Nanoparticles with Tunable Size and Surface Plasmon Resonance Frequency. *Chem. Mater.* **2011**, *23*, 4098−4101.
(13) Monga, A.; Pal, B. Improved Catalytic Activity and Surface Electro-Kinetics of Bimetallic Au-Ag Core-Shell Nanocomposites. *New J. Chem.* **2015**, *39*, 304−313.
(14) Papagiannouli, I.; Aloukos, P.; Rioux, D.; Meunier, M.; Couris, S. Effect of the Composition on the Nonlinear Optical Response of $Au_xAg_{1-x}$ Nano-Alloys. *J. Phys. Chem. C* **2015**, *119*, 6861−6872.
(15) Shin, K. S.; Kim, J. H.; Kim, I. H.; Kim, K. Novel Fabrication and Catalytic Application of Poly(ethylenimine)-Stabilized Gold-Silver Alloy Nanoparticles. *J. Nanopart. Res.* **2012**, *14*, 735.
(16) Sun, Y. G.; Xia, Y. N. Mechanistic Study on the Replacement Reaction between Silver Nanostructures and Chloroauric Acid in Aqueous Medium. *J. Am. Chem. Soc.* **2004**, *126*, 3892−3901.
(17) Tsuji, M.; Kidera, T.; Yajima, A.; Hamasaki, M.; Hattori, M.; Tsuji, T.; Kawazumi, H. Synthesis of Au-Au and Ag-Pd Alloy Triangular Hollow Nanoframes by Galvanic Replacement Reactions without and with Post-Treatment using NaCl in an Aqueous Solution. *CrystEngComm* **2014**, *16*, 2684−2691.
(18) Li, W. Z.; Kuai, L.; Chen, L.; Geng, B. Y. Re-growth Etching" to Large-sized Porous Gold Nanostructures. *Sci. Rep.* **2013**, *3*, 2377.
(19) Mallin, M. P.; Murphy, C. J. Solution-Phase Synthesis of Sub-10 Nm Au-Ag Alloy Nanoparticles. *Nano Lett.* **2002**, *2*, 1235−1237.
(20) Link, S.; Wang, Z. L.; El-Sayed, M. A. Alloy Formation of Gold-Silver Nanoparticles and the Dependence of the Plasmon Absorption on Their Composition. *J. Phys. Chem. B* **1999**, *103*, 3529−3533.
(21) Kim, K.; Kim, K. L.; Lee, S. J. Surface Enrichment of Ag Atoms in Au/Ag Alloy Nanoparticles Revealed by Surface Enhanced Raman Scattering Spectroscopy. *Chem. Phys. Lett.* **2005**, *403*, 77−82.
(22) Manzhos, R. A.; Krivenko, A. G.; Doronin, S. V.; Choba, M. A.; Safonov, V. A. Surface Segregation of Silver Atoms on Au-Ag Alloys According to Data of Laser-Heating Induced Temperature Potential Shifts, XPS and Conventional Electrochemical Methods. *J. Electroanal. Chem.* **2013**, *704*, 175−182.
(23) Deng, L.; Hu, W.; Deng, H.; Xiao, S.; Tang, J. Au-Ag Bimetallic Nanoparticles: Surface Segregation and Atomic-Scale Structure. *J. Phys. Chem. C* **2011**, *115*, 11355−11363.
(24) Kim, K.; Kim, K. L.; Choi, J.-Y.; Lee, H. B.; Shin, K. S. Surface Enrichment of Ag Atoms in Au/Ag Alloy Nanoparticles Revealed by Surface-Enhanced Raman Scattering of 2,6-Dimethylphenyl Isocyanide. *J. Phys. Chem. C* **2010**, *114*, 3448−3453.
(25) Rajendra, R.; Bhatia, P.; Justin, A.; Sharma, S.; Ballav, N. Homogeneously-Alloyed Gold-Silver Nanoparticles as per Feeding Moles. *J. Phys. Chem. C* **2015**, *119*, 5604−5613.
(26) Kim, S. W.; Kim, M.; Lee, W. Y.; Hyeon, T. Fabrication of Hollow Palladium Spheres and Their Successful Application to the Recyclable Heterogeneous Catalyst for Suzuki Coupling Reaction. *J. Am. Chem. Soc.* **2002**, *124*, 7642−7643.
(27) Chen, H. M.; Liu, R. S.; Lo, M. Y.; Chang, S. C.; Tsai, L. D.; Peng, Y. M.; Lee, J. F. Hollow Platinum Spheres with Nano-Channels: Synthesis and Enhanced Catalysis for Oxygen Reduction. *J. Phys. Chem. C* **2008**, *112*, 7522−7526.
(28) Zeng, J.; Zhang, Q.; Chen, J. Y.; Xia, Y. N. A Comparison Study of the Catalytic Properties of Au-based Nanocages, Nanoboxes, and Nanoparticles. *Nano Lett.* **2010**, *10*, 30−35.
(29) Wu, H. X.; Wang, P.; He, H. L.; Jin, Y. D. Controlled Synthesis of Porous Ag/Au Bimetallic Hollow Nanoshells with Tunable Plasmonic and Catalytic Properties. *Nano Res.* **2012**, *5* (2), 135−144.
(30) Sandhyarani, N.; Pradeep, T. Crystalline Solids of Alloy Clusters. *Chem. Mater.* **2000**, *12*, 1755−1761.
(31) Alissawi, N.; Zaporojtchenko, V.; Strunskus, T.; Kocabas, I.; Chakravadhanula, V. S. K.; Kienle, L.; Garbe-Schönberg, D.; Faupel, F. Effect of Gold Alloying on Stability of Silver Nanoparticles and Control of Silver Ion Release from Vapor-Deposited Ag-Au/Polytetrafluoroethylene Nanocomposites. *Gold Bull.* **2013**, *46*, 3−11.
(32) Jang, H.; Min, D.-H. Spherically-Clustered Porous Au-Ag Alloy Nanoparticle Prepared by Partial Inhibition of Galvanic Replacement and Its Application for Efficient Multimodal Therapy. *ACS Nano* **2015**, *9* (3), 2696−2703.
(33) Singh, S.; D'Britto, V.; Prabhune, A. A.; Ramana, C. V.; Dhawan, A.; Prasad, L. V. Cytotoxic and Genotoxic Assessment of Glycolipid-Reduced and − Capped Gold and Silver Nanoparticles. *New J. Chem.* **2010**, *34*, 294−301.
(34) Shin, K. S.; Kim, J. H.; Kim, I. H.; Kim, K. Novel Fabrication and Catalytic Application of Poly(ethylenimine)-Stabilized Gold-Silver Alloy Nanoparticles. *J. Nanopart. Res.* **2012**, *14*, 735.
(35) Fa, W.; Zhou, J.; Dong, J. M. First-Principles Simulations on Suspended Coinagemetal Nanotubes Composed of Different Atomic Species. *Phys. Chem. Chem. Phys.* **2013**, *15*, 4610−4615.
(36) Wu, Y.; Jiang, P.; Jiang, M.; Wang, T.-W.; Guo, C.-F.; Xie, S.-S.; Wang, Z.-L. The Shape Evolution of Gold Seeds and Gold@Silver Core-Shell Nanostructures. *Nanotechnology* **2009**, *20*, 305602.
(37) Strasser, P. Catalysts by Platonic Design- Sophisticated Shape-Controlled Design is Yielding Ever More Active Nanocatalysts. *Science* **2015**, *349* (6246), 379−380.
(38) Stephens, E. L. I.; Elias, J. S.; Yang, S.-H. The Importance of Being Together-Controlling the Coordination of Platinum Boosts Catalytic Reaction Rates. *Science* **2015**, *350* (6257), 164−165.
(39) Wan, Y.; Guo, Z. R.; Jiang, X. L.; Fang, K.; Lu, X.; Zhang, Y.; Gu, N. Quasi-Spherical Silver Nanoparticles: Aqueous Synthesis and Size Control by the Seed-Mediated Lee-Meisel Method. *J. Colloid Interface Sci.* **2013**, *394*, 263−268.


DOI: 10.1021/acsami.6b03728
*ACS Appl. Mater. Interfaces* 2016, 8, 16833−16844